Eur. Phys. J. B **11**, 327–343 (1999)

THE EUROPEAN PHYSICAL JOURNAL B

EDP Sciences

Mechanisms of CVD diamond nucleation and growth on mechanically scratched Si(100) surfaces

J.C. Arnault, L. Demuynck, C. Speisser, and F. Le Normand[a]

Groupe Surfaces-Interfaces, Institut de Physique et Chimie des Matériaux (IPCMS-GSI)[b], Bâtiment 69, 23 rue du Loess, 67037 Strasbourg Cedex, France

Received 21 December 1998

Abstract. The diamond nucleation has been studied on scratched Si(100) both by surface analyses (XPS, AES, ELS) and microstructural probes (AFM, SEM). Two pathways for diamond formation and growth are detected: A *seeding pathway* occurs by direct growth from part of diamond seeds left by the mechanical pretreatment. Not all of these seeds however are prone to diamond growth as they can be either dissolved or carburized. A *nucleation pathway* occurs through a stepwise process including the formation of extrinsic (pretreatment) or intrinsic (*in situ*) nucleation sites, followed by formation of carbon-based precursors. It is believed that nucleation sites could be either grooves of scratching lines or protrusions produced by etching-redeposition. The size of these protrusions is not larger than 100 nm. On top of these protrusions as well as on the bare substrate, a thin layer of silicon carbide rapidly forms and DLC carbon likely. This complex process on top of protrusions may constitute carbon-based embryos for further diamond nucleation.

PACS. 81.05.Tp Fullerenes and related materials; diamonds, graphite – 81.15.Gh Chemical vapor deposition (including plasma-enhanced CVD, MOCVD, etc.) – 82.65.-i Surface and interface chemistry

1 Introduction

The successful growth of diamond films *via* Chemical Vapor Deposition (CVD) has stimulated an enormous interest due to the outstanding properties of diamond for present or new technological applications [1]. The good electrical insulation, high thermal conductivity and low dielectric constant make diamond well-suited for use in device packaging and multichip module technologies; the extreme hardness and wide optical band gap provide an excellent material for optical or opto-electronic applications; the chemical inertness and the high hardness make it ideal for protective coating against corrosion and wear in cutting tools as well. Nevertheless, the most powerful development would be an electronics based on diamond running in harsh thermal, corrosive or radiative environments, owing to its unique electronic properties. The combination of such properties requires however to grow high quality, strongly adhesive as well as properly doped diamond films. Unfortunately many earlier attempts to grow diamond on non-diamond substrates have yielded poorly adhesive polycrystalline films, obtained by 3D growth of randomly-oriented crystals containing non-diamond carbons and other impurities as well as structural defects. One main reason for this feature is the poor basic understanding of the nucleation and the growth at the early stages of diamond deposition. Nevertheless, there has been a considerable amount of work to elucidate the mechanisms of CVD diamond nucleation and growth, since the pioneering work by Matsumoto *et al.* using the Hot Filament (HFCVD) process [2].

Let us outline some of the prominent results that merge from the prolific literature devoted to these topics. It is now clearly established that the CVD diamond synthesis requires the occurrence of *surface defects* [3,4]. Defects are needed to induce the nucleation process by lowering the enthalpy of nuclei formation [5], as it has been claimed in the current theories of nucleation [6–8]. Indeed accurate patterning treatments clearly lead to preferential nucleation on top of tips or whiskers [9,10]. However generally both the real chemical and the intimate structural nature of such defects relevant to nucleation are still a matter of debate. Mechanical scratching and ultrasonic agitation treatments lead to high density polycrystalline films with randomly oriented diamond nuclei. However, no obvious relationship is found between the scratches and the diamond particles, although this has been sometimes reported, *e.g.* along the edges of Si(111) terraces [11]. Furthermore it is claimed that *diamond seeds* left on the substrate after the mechanical polishing act as germs for further diamond growth [12,13]. *In situ* etching of the substrate can also dramatically enhance

[a] e-mail: `fln@odhinn.u-strasbg.fr`
[b] UMR 7504 du CNRS

the nucleation. Applying a negative bias during a short preliminary treatment successfully achieves the highest density presently observed together with clear preferential orientation of the nuclei [14]. The *transformation between various allotropic forms of carbon* and the *chemical nature of the substrate* must also be addressed to understand the stepwise formation of nucleation sites, embryos and nuclei. Thus preferential nucleation occurs on the edges of graphitic prismatic planes [15], a process that has been further modelized by molecular simulations [16]. Moreover, high nucleation density has been reported on Si and other refractory metals where a carbide formation could be observed [17,18], while both a poor nucleation density and a slow nucleation rate were reported on metals unable to form carbides or to dissolve carbon (Cu, Pt, Au, Ni, ...) [19,20]. To sort out among these likely processes, there is a need for more basic and comprehensive studies of diamond nucleation and growth on well-characterized surfaces. In a parallel work [21], we have established that nucleation on virgin Si(111) and Si(100) surfaces occurs *via* a three step process including (i) first the selective formation of defects of well-defined symmetry through etching by hydrogen radicals which provide suitable nucleation sites, (ii) subsequent stabilization of embryos on these sites and finally (iii) formation of nuclei. This interpretation can be described by the phenomenological kinetic model first developed by Molinari *et al.* [22], recently extended to the initial step of defects formation [23]. By contrast, there are only few studies that describe the nucleation process when preliminary treatments are applied to the silicon substrate in order to significantly increase the nucleation density. These widely used treatments include mechanical polishing [24,25], mechanical abrasion with ultrasonic agitation [26] or ion impingement *via* a negative bias applied between the substrate and the activation source [27].

The aim of this work is to study the nucleation and growth processes of CVD diamond on a mechanically scratched Si(100) surface and to compare with the results obtained on virgin Si(100). The scratching treatment is implemented by polishing with diamond paste (1/4 μm), where surface structural defects are generated along randomly distributed lines. The experiments are performed in a synthesis chamber directly connected to another chamber, enabling to sequentially monitor the diamond nucleation and growth by surface analyses including X-ray photoemission (XPS), Auger electrons (AES) and Electron Losses (ELS) spectroscopies without breaking the vacuum. Deposits on separate samples were performed under similar conditions for microstructural investigations including Scanning Electron (SEM), Atomic Force (AFM) and Transmission Electron (TEM) microscopies. The main results of this study can be summarized as follows:

- Two pathways are proposed to occur on silicon that lead to diamond growth.
- The first one is a germ pathway which involves a part of the diamond seeds left by the pretreatment of the substrate.
- The second one is a stepwise nucleation pathway that involves subsequent preliminary formation of nucleation sites and carbon-based embryos on it. It therefore requires an incubation time.
- It is proposed that the nucleation site is mainly silicon protrusion generated by the etching of the material. On top of these protrusions, silicon carbide and amorphous DLC carbon are formed that constitute the carbon embryos.

2 Experimental part

2.1 Sample and CVD conditions

The samples were prepared by polishing a Si(100) wafer supplied by Wacker with diamond paste (15, 10, 3, 1 and finally 1/4 μm). The boron-doped silicon samples of resistivity 17−23 Ωcm were first ultrasonically cleaned in CCl_4 and ethanol solutions, before being introduced into the preparation chamber. The only surface impurities that could be detected by AES were carbon and oxygen. Unless otherwise stated, no *in situ* vacuum surface treatment such as Ar^+ ion etching or thermal treatment was attempted, in order to preserve the defects and the germs left by the scratching procedure. It will further be observed that such treatments strongly affect the nucleation density.

The CVD diamond was grown by the hot filament process (HFCVD) which activates a gas mixture of hydrogen of grade 5.5 and methane (0.5%). The deposition was carried out in ultra high vacuum stainless steel chamber with a base pressure of 10^{-9} mbar. The tungsten filaments, set at a distance d between 5 and 7 mm above the sample surface, were heated at 2400 ± 25 K, corresponding to an electric power into the filaments of 185 ± 5 Watt. The temperature of the substrate was 1073 ± 10 K. The total pressure was 3000 Pa and the gas flow was 200 l/min. More details on the CVD chamber were reported in reference [28]. Besides, the procedures (i) to reach steady state deposition conditions, (ii) to stop a deposition sequence and (iii) to transfer the sample for surface analyses have been elsewhere described [21]. Both sequential and continuous depositions were carried out for spectroscopic and microstructural investigations, respectively. We checked that these two procedures lead to similar nucleation density and growth law, under identical gas and sample conditions.

2.2 Surface analyses

The standard conditions of the surface analyses by electron spectroscopies have been reported elsewhere [29]. Shortly, the UHV chamber was a custom-built system equipped with a VSW 100 mm hemispherical analyzer. The base pressure was 10^{-10} mbar in the chamber and 5×10^{-10} mbar during the analyses. Photoelectrons, Auger electrons and inelastic electrons were collected when escaping from a direction quasi-normal to the surface of the substrate.

The X-ray source was an unmonochomatized PHI Mg anode providing photons of 1253.6 eV kinetic energy with an angle of incidence of 30°. The acceleration voltage was 13 kV and the power was 300 Watt. The resolution was then 0.60 eV, as measured by the broadening of the $4f7/2$ line of a clean gold foil. The binding energies were referred to the calibration of core levels of clean copper, silver and gold foils (75.14, 83.98, 368.26 and 932.67 eV for the Cu $3p$, Au $4f7/2$, Ag $3d5/2$ and Cu $2p3/2$ levels, respectively). The XPS intensity of each individual contribution was calculated by the use of a model previously reported [26].

The AES spectra were recorded in the derivative mode $\mathrm{d}N(E)/\mathrm{d}E$ with a kinetic energy of the primary electrons of 1 keV and a modulation of 4 V.

For ELS, the electron beam energy was either 250 eV or 1200 eV. The electron escape depth of the elastically scattered electrons is then estimated to 7.4 Å and to 16.2 Å, respectively [30]. The spectra were recorded with an energy resolution of 1 eV from a sampling area of about 2 mm^2 and the intensities were normalized to the elastic peak. We checked the absence of electron beam induced damages such as carbon amorphization or carbon transformation. We frequently changed the area analyzed in order to check the homogeneity of the deposit.

2.3 Structural investigations

SEM investigations were performed on a JEOL JSM 840 set up. The images were recorded at 10 or 15 kV with a resolution estimated to 0.05 μm. Image treatments and analyses were performed using a home-made program extracted from the KHOROS freeware. This allows to determine the covered surface S and the nucleation density N. A difficulty arises however when the particles display re-entrant corners leading to concave surfaces. This morphology could be due either to the aggregation of impinging particles which do not coalesce at a temperature too low for carbon migration, or to different growth directions generated after a stacking fault. Such a defect is frequently observed in diamond growth. Therefore, the procedure counts the whole aggregated ensemble. A mean diameter D is further calculated by the equation (1)

$$D = 2A[S/(N\pi)]^{1/2} \tag{1}$$

where A is a geometrical factor accounting for the mean shape of a diamond particle. Assuming an hexagonal shape as the more usual shape, A quotes to 0.83. More details on the counting procedure were reported in reference [26]. Several hundred islands were counted for each sample.

AFM observations were performed at ambient atmosphere, on a Nanoscope III multimode microscope from Digital Instruments. The vibrating tapping mode was preferred to the contact mode because of the strong interaction of the AFM tip with the diamond islands. During the scan, the tip-surface distance was of several nanometers so that the interaction with the surface was minimized. In this particular mode, a silicon cantilever vibrated near its resonance frequency (290−420 kHz) with a nominal spring constant within 20−100 N/m. The effect of the force gradient on the vibration amplitude was measured *via* optical detection. By use of an optimized feedback loop, topographic images of the sample surface were recorded. The sharpest tips were selected with an estimated nominal radius of curvature within 5-10 nm.

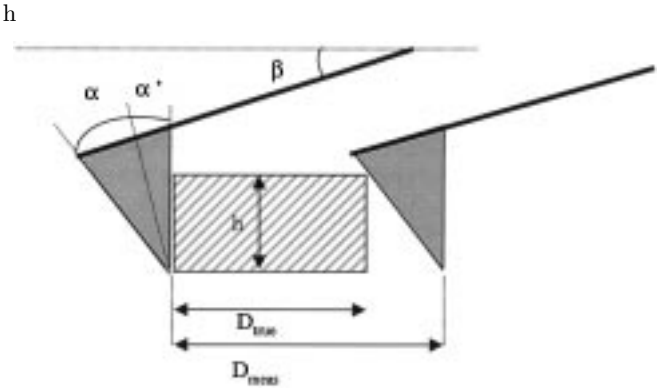

Scheme 1. AFM tip effect on the measurement of the lateral size of a cubic grain.

From the AFM recorded images, the roughness of the surface topography was calculated. The standard deviation of the height values, noted R_q, was obtained as follows:

$$R_\mathrm{q} = [1/N \sum_i (Z_i - Z_\mathrm{m})^2]^{1/2}, \text{ for } i \text{ from 1 to } N \tag{2}$$

where Z_m is the average of the Z values within the given image, Z_i is the current Z value and N is the number of points of the image.

In AFM, one has to consider the convolution of the tip with the surface for the lateral resolution. Therefore, the effect was corrected by taking into account the tip shape [31]. In the tapping mode, the silicon tip had cone half angles $\alpha = 25°$ and $\alpha' = 10°$, at the front and at the back, respectively. The cantilever direction had an angle β close to 10°, with the horizontal. Assuming a cubic shape for the diamond islands, it is easy to demonstrate the relation (3) between the measured and the true lateral size, D_meas (nm) and D_true (nm) respectively, taking into account the height of the island h (nm) (Scheme 1):

$$D_\mathrm{true} = D_\mathrm{meas} - h[\tan(\pi/2 - \beta - \alpha)]^{-1} \tag{3}$$

which for $\alpha = 25°$, $\beta = 10°$ reduces to (4):

$$D_\mathrm{true} = D_\mathrm{meas} - 0.7h. \tag{4}$$

Some samples were prepared for TEM examination by the extractive replica technique. After coating of the surface by evaporation of an amorphous carbon layer, the silicon support is dissolved in a HF: CH_3COOH: HNO_3 solution (1:3:2 vol). The thin film including the carbon islands is then collected on a 1000 mesh copper grid. It has been shown that such preparation allows to observe the whole deposit [29].

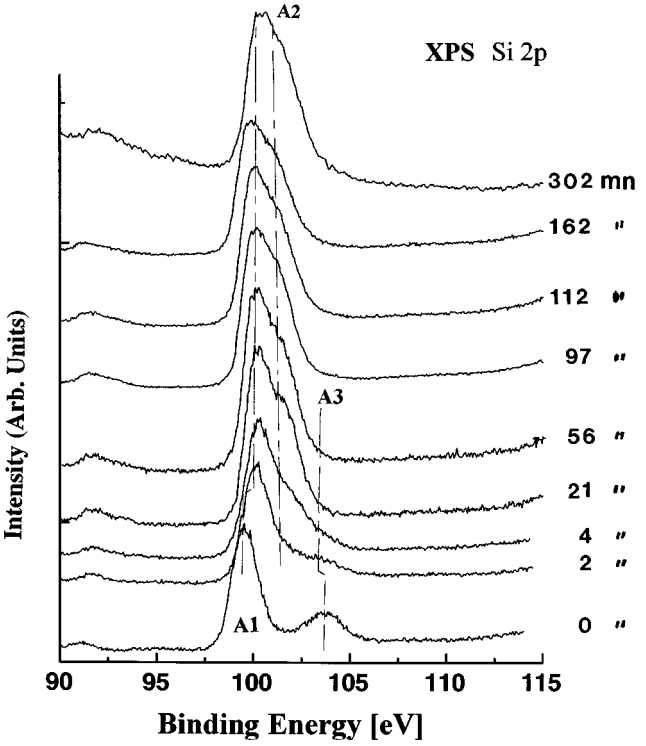

Fig. 1. Evolution of the Si $2p$ core level with the cumulative deposition time. The assignment of the A_1, A_2 and A_3 components is discussed in the text. The intensity scale is not normalized.

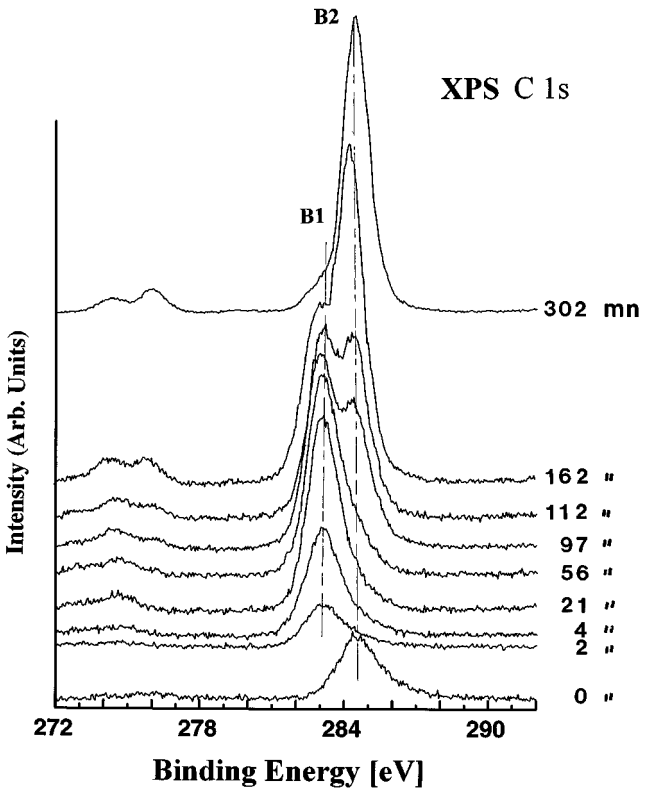

Fig. 2. Evolution of the C $1s$ core level with the cumulative deposition time. The assignment of the B_1 and B_2 components is discussed in the text. The intensity scale is normalized.

3 Results

3.1 Surface analyses

3.1.1 XPS

The surface of the initial substrate is oxidized, so that in the Si $2p$ core level a large oxide contribution SiO_x (A_3) emerges around 104 eV beside the elemental silicon (A_1) at 99.6 eV (Fig. 1). This oxide contribution disappears after the first deposition sequence, this being consistent with a sharp drop of the oxygen O $1s$ signal (not shown).

A new feature (A_2) at 101.9 eV is detected as a shoulder of the main silicon contribution A_1. This new feature becomes clearly visible as early as 21 min deposition time. It may be assigned to silicon carbide [32,33]. After 21 min of deposition, we only detect these two contributions with a relative ratio that does not change very much. For the C $1s$ core level (Fig. 2), the broad initial peak denoted B_2 at 284.6 eV corresponds both to contamination carbon and to hard carbon grains left by the scratching process. Attempts to clean the silicon surface from contamination carbon by vacuum annealing above 1023 K are unsuccessful in the present case. This result, together with AFM investigations described below, supports the assumption of the actual presence of carbon residues on the initial surface. Such residues have been first detected by TEM by Iijima [12]. Subsequent sequences of carbon deposition lead to two contributions. The first one denoted B_1 at low binding energy (283.15 eV) is the most intense up to about 115 min and can clearly be assigned to silicon carbide formation [33]. Furthermore, we note that the binding energy difference between the B_1 feature of the C $1s$ core level and the A_2 feature of the Si $2p$ core level, both assigned to the silicon carbide compound, is 182.25 ± 0.1 eV, in good agreement with the 182.15 eV difference reported elsewhere for silicon carbide [34]. The second contribution B_2 at 284.6 eV is initially very weak, but is rapidly increasing. It can clearly be detected above 56 min and becomes the unique one above 302 min. We attribute it to diamond

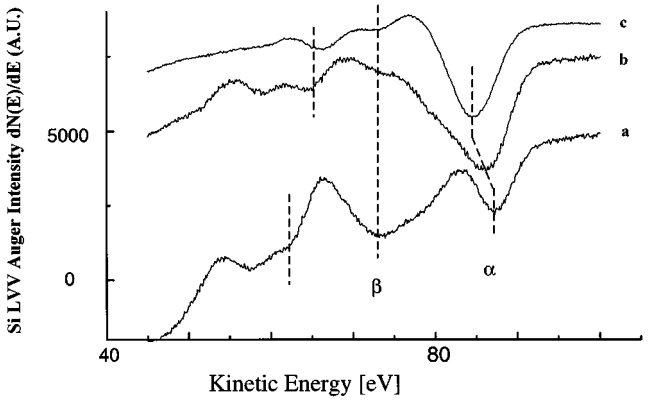

Fig. 3. Typical spectra of the Si LVV transition ($d(N(E)/dE$ mode) as a function of the cumulative deposition time. The assignment of the α and β features is discussed in the text.

or to amorphous carbon, as reported in the literature [34,35]. Let us note that, whatever the real nature of elemental carbon (graphitic, amorphous, diamond, ...), a single line is obtained around 284.6 eV with a resolution not less than 0.6 eV [34]. The nature of this carbon species can therefore hardly be assessed using XPS alone. Both AES and ELS in addition are necessary to further investigate the nature of this elemental carbon. More details on the exploitation of these XPS spectra were elsewhere reported [32].

3.1.2 AES

Some characteristic Auger spectra of the Si $L_{2,3}VV$ transition in the $dN(E)/dE$ mode are presented (Fig. 3) at different deposition times. They display clear modifications of the shape which can be attributed to modifications of the silicon bonding state. The peaks will be labeled according to the energy of their minimum derivative feature.

The initial spectrum clearly confirms the presence of an oxide layer with a broad minimum β around 73 eV and associated satellites at 62.3 and 57 eV (Fig. 3a). We also observe an elemental silicon contribution α at 87.4 eV. From the relative intensities at the silicon oxide and silicon peaks, the equivalent depth of oxide layer can be estimated to $\approx$ 1.5 nm [36]. These minima are slightly shifted to lower kinetic energies than previously reported (by about 1.5 eV), but this can be attributed to contamination carbon also covering the substrate. A first deposition sequence (2 minutes) leads to an almost complete reduction of the oxide as ascertained by the large drop of the minimum β at 73.1 eV (Fig. 3b). Furthermore, the silicon minimum shifts by about 3 eV towards lower kinetic energies. This is quite characteristic of silicon carbide formation [37]. The spectra do not significantly evolve after 20 minutes (Fig. 3c), still displaying a very small contamination by oxygen.

For the C KVV transition (Fig. 4), the initial structureless and very broad shape around 265 eV is indicative of amorphous carbon (Fig. 4a). As stated above, this amorphous carbon is mainly due to contamination carbon, but also to some carbon residues left on the surface by the mechanical scratching. Strong modifications of the spectrum occur after 2 min of deposition (Fig. 4b). The main minimum of the transition shifts towards higher kinetic energies by about 3.5 eV. Fine structures now appear at 248.1 eV (noted a_3) and 240.1 eV (noted a_4). The shape of the spectrum is quite comparable to that of the silicon carbide reference published by Parrill and Chung [33]. In agreement with their interpretation, a_3 is assigned to an Auger transition whereas a_4 is a loss contribution accompanying the main Auger transition. Later on, the evolution with deposition time is weak and we only note a narrowing of the main component together with a better definition of fine structures. The spectrum after 80 min clearly exhibits the fine structures a_1, a_2 and a_3 at 259.7, 255.2 and 248.1 eV, respectively (Fig. 4c). These are separated by 5.8 eV, 10.3 eV and 17.4 eV, respectively, from the main minimum S at 265.5 eV. They are clearly attributed to

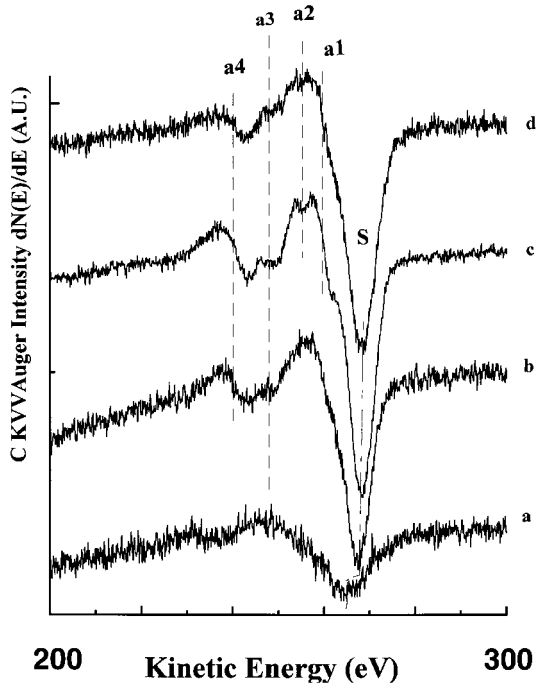

Fig. 4. Typical spectra of the C KVV transition as a function of the cumulative deposition time. The assignment of the a_1, a_2, a_3 and a_4 features is discussed in the text.

Auger transitions of the silicon carbide. A loss feature a_4 again points out at 240.2 eV. After 220 min of deposition however, we do observe some changes (Fig. 4d). The intensities of the a_2, a_3 and a_4 features decrease, while the feature a_1 shifts upwards and now appears as a shoulder of S. This shape indicates now a mixture of diamond and silicon carbide.

3.1.3 ELS

Electron loss spectra, recorded at two kinetic energies of the electrons, in order to be surface sensitive, also indicate quite significant modifications of the surface.

Figure 5A displays electron loss spectra recorded at 250 eV. The initial surface yields an intense and broad structure at 22.5 eV (Fig. 5Aa). In agreement with Si LVV and Si 2p spectra, this is mainly attributed to the bulk plasmon of silicon dioxide $\omega_B^{SiO_2}$. There is also a weak feature around $16.5 - 17$ eV. This could be assigned to the bulk plasmon of silicon ω_B^{Si} or to the surface plasmon associated to silicon dioxide $\omega_S^{SiO_2}$. The small initial contribution of the π states at 6.8 eV supports the presence of amorphous carbon contamination that is partially unsaturated.

After a first deposition sequence (4 min), the silicon bulk plasmon ω_B^{Si} is more pronounced and the main feature peaking now at 21.6 eV is narrower (Fig. 5Ab). This can be interpreted by two effects of the hydrogen and hydrocarbon radicals : (i) reduction of the silicon oxide layer and formation of silicon carbide whose bulk plasmon

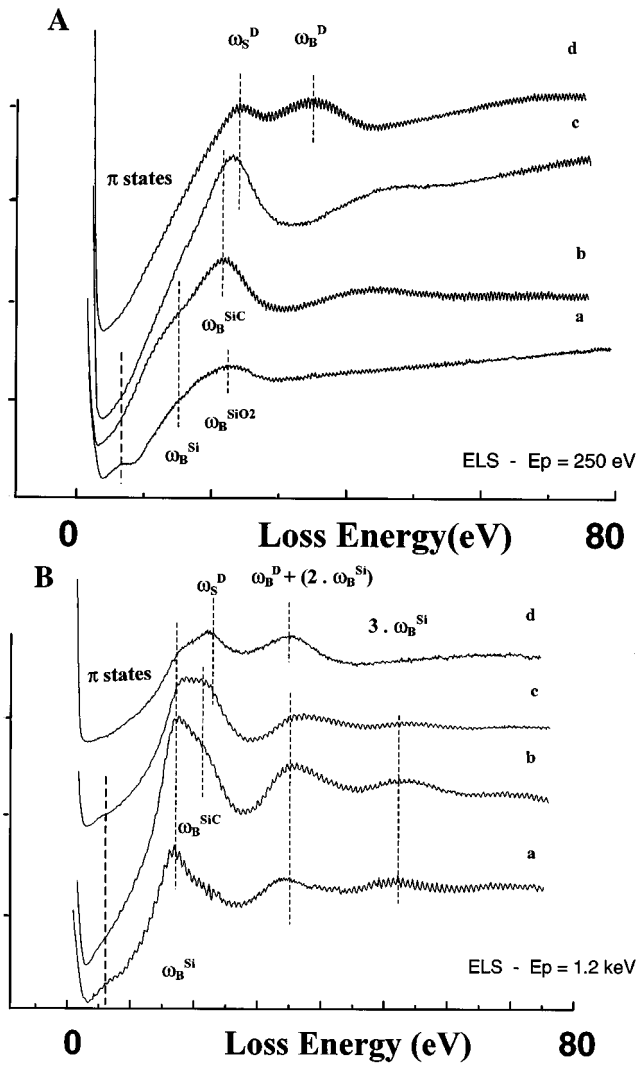

Fig. 5. Electron loss spectra at A) $E_p = 250$ eV and B) $E_p = 1200$ eV as a function of the cumulative deposition time.

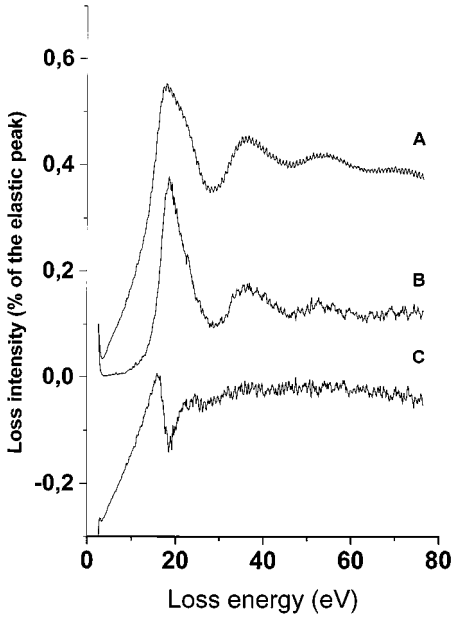

Fig. 6. Electron loss spectra on A) scratched Si(100); B) virgin Si(100) taken from reference [21] and C) difference spectra (A – B). The intensities are normalized to the elastic peak. The spectra are recorded at similar I_C/I_{Si} XPS ratio, corresponding to 4 min and 80 min of deposition times on the scratched and virgin samples, respectively.

peaks around 21 eV [33]. The contribution of the carbon π states almost disappears. Thus, within the limits of sensitivity of the ELS probe, we can stress that surface carbon is quickly saturated (sp^3 hybridization) as soon as the CVD conditions are established. Further depositions up to 80 min lead to the shift of the silicon carbide contribution towards 23 eV. This can be due to a mixing with a surface plasmon of diamond ω_S^D. The diamond surface ω_S^D and bulk ω_B^D plasmons occur at 23.5 and 34.3 eV, respectively, and dominate after 302 min of deposition, with a ratio ω_B^D/ω_S^D of 1.46 (Fig. 5Ad).

ELS spectra recorded at $E_p = 1200$ eV are displayed in Figure 5B for identical deposition times. There is no obvious difference in the initial spectrum with that recorded at 250 eV, apart from the more intense bulk plasmon of the silicon at 17 eV (Fig. 5Ba). We also clearly note the first and the second harmonics of the silicon bulk plasmon $2\omega_B^{Si}$ and $3\omega_B^{Si}$ at 35.2 et 52.8 eV, respectively. The first 4 min deposition confirms the apparition of the bulk silicon carbide ω_B^{SiC} at 21.3 eV, but the silicon feature ω_B^{Si} is still detectable. A main difference between the 250 eV and the 1200 eV ELS spectra is that in the latter case we still detect a weak contribution of unsaturated carbon π_C at 6.5-7 eV (Fig. 5Bb). The broadening observed after 80 min of deposition can be assigned to a mixture of the three contributions ω_B^{si} (17 eV), ω_B^{SiC} (21 eV) and ω_S^D (23 eV) (Fig. 5Bc). The last spectrum (Fig. 5Bd) is dominated by the two diamond losses ω_S^D and ω_B^D while the silicon bulk plasmon ω_B^{Si} is still clearly detectable.

In an attempt to get more information on the real nature of the carbon species involved, we compare the 250 eV ELS spectra of a scratched and of a virgin Si(100), reported elsewhere [21] (Fig. 6). The energy range of interest is 5–15 eV, where it is believed that electron losses are only sensitive to the carbon state. The difference spectrum of the normalized ELS spectra is recorded at similar C/Si intensities ($I_C/I_{Si} = 0.4$). It exhibits in this energy range a more intense contribution of the scratched sample. This can already be seen in the original ELS spectra, where the flat bottom of the virgin sample (Fig. 6B) contrasts with the continuously rising losses of the scratched sample (Fig. 6A). This increase can be ascribed to partially amorphous or defective carbon, such that the lack of long-range order induces a breakdown in the dipolar selection rules and yields a continuum of empty carbon states [38]. Both the negative contribution around 18 eV and the positive contribution around 21 eV are attributed to a more intense ω_B^{Si} signal on the virgin sample, indicative that the SiC layer is randomly thicker on the scratched sample than on the virgin sample, a point that will be further confirmed.

3.2 Microstructural investigations

Some typical SEM and AFM pictures are depicted for different deposition times in Figures 7 and 8, respectively. With sufficient resolution, these images outline three main features:

- Scratching lines due to the surface treatment. They are seen by AFM and SEM on every substrate, suggesting a good stability of this damage within the deposition conditions. They are randomly oriented. Their width is estimated to 50–100 nm whereas their depth does not exceed 10 nm.

- Growing nuclei of diamond whose mean size increases with time. They are generally well facetted. Aggregated-like particles are clearly observed above 180 min. Their size distribution is rather homogeneous at $t > 120$ min, but more dispersed at lower deposition times. A preferential distribution of the growing nuclei along scratches is sometimes observed, but there is no obvious and general relationship between these two features. We decided not to report the size distribution, owing to the inhomogeneity of the size below 120 minutes and the presence of aggregated-like diamond islands above 180 minutes. Furthermore, it is believed that the surface coverage rather than a mean diameter or a size distribution is the relevant parameter for a further description of the diamond growth.

- Although sometimes barely detectable by SEM, we evidence a population of very small particles. The populations of growing nuclei and small particles are more efficiently detected by AFM, for example in Figure 8f corresponding to $t = 180$ min. However difficulties arise (i) to count and to measure them because of the limited lateral resolution of the AFM microscope and (ii) to define a size criterion by which we will separate these small islands from the growing nuclei. Fortunately, the mean size of such small particles is rather homogeneous ranging between 0.05 and 0.09 μm, whereas facetted diamond nuclei exceed 0.1 μm size. We therefore arbitrarily separate these two populations as follows: small particles are those whose mean size is lower than 0.1 μm, whereas growing nuclei are particles whose size exceeds 0.1 μm. Another remarkable result is that the mean size of these particles remains stable with time. Even after 180 minutes, we clearly distinguish this population which coexists with highly-facetted diamond growing nuclei in the vicinity. By contrast they do not seem well-facetted, although a clear evidence of a facetting becomes hard to obtain by AFM in the range 0.05−0.1 μm. We also note that there is no systematic trend as far as the localization of these small particles and the scratches is concerned, although there is some marked presence at the intersect of two scratches or along some scratches (arrows in Fig. 8b and 8e, respectively). Finally, many attempts to observe by HRTEM these small particles are up to now unsuccessful, by contrast with diamond and silicon carbide.

The analyses of SEM micrographs allows us to determine the diamond nucleation density N and the covered surface S (the surface fraction occupied by diamond islands). The nucleation density N again as well as the roughness R_q, the heights h of small particles and growing nuclei can be extracted from AFM images. A lateral size D_{meas} can also be deduced from the AFM scan lines. However, further use of D_{meas} requires to be aware of two physical perturbations inherent to AFM measurements. Firstly, the measured in-plane size D_{meas} is the convolution of the real size with the tip radius of curvature. Secondly, the critical response of the electronic feedback is hardly recorded when an abrupt change of slope occurs such as on well-facetted diamond particles. These two effects cause usually an overestimation of the diameter D_{meas} which has been well described in the literature [31]. Moreover the well-facetted character of the diamond particles also introduces multiples errors on the measurement of both h and D_{meas}, depending on the position of the extracted line scan with respect to the facet. These limitations are much less effective for small particles which exhibit a rounder morphology and a smoother change of slope, hence only a tip effect really occurs. Thus, as previously stated, a correction of the AFM images is done by considering the tip geometry (Scheme 1 and Eqs. (3) and (4)). In this way, more realistic lateral sizes D_{true} are extracted.

Considering that the growth of 3D diamond islands is a phase transformation process as determined on copper [28,31], we apply the kinetics of such transformations taking into account the mutual interference of areas growing from separate nuclei. The fraction of the logarithm of the uncovered surface $(1 - S)$ has been plotted *versus* deposition time in a Ln-Ln plot (Fig. 9). The experimental points, determined by analyses of the SEM pictures, were fitted according to Avrami's formalism [39]:

$$S = [1 - \exp(-kt^n)] \tag{5}$$

where the slope gives directly the exponent n of expression (5) and k is a kinetic rate constant. The plot exhibits a two-step behaviour with a clear breakpoint around $t \approx 45$ minutes. Beyond this breakpoint, the slope of the curve is about 0.5, which is indicative of a diffusion-controlled growth of small platelets [40]. It should be noted that the covered surface is not zero initially as we do observe some particles on the initial surface. Above 45 minutes, the slope jumps to 2.8 ± 0.15. This is quite relevant to the nucleation and growth of a tridimensional phase where the growth is governed by the direct chemical reactivity from the gas phase and the nucleation rate is slightly decreasing with time. It is particularly instructive to compare this result with virgin Si(100) [21]. After a much longer incubation time corresponding to 120 minutes, the virgin Si(100) exhibits a quite similar slope.

The variation of the density of growing diamond nuclei N, taken as the mean value of the SEM and AFM countings, is displayed in Figure 10. It exhibits a small incubation time followed by a fast increase up to a maximum around 120 minutes above 10^{-8} cm^{-2}. Further, the slight decrease of the nucleation density is due to the aggregation process of the particles that overcomes the decreasing rate of nucleation. We also display the density of small particles n on the area uncovered by diamond islands $(1 - S)$,

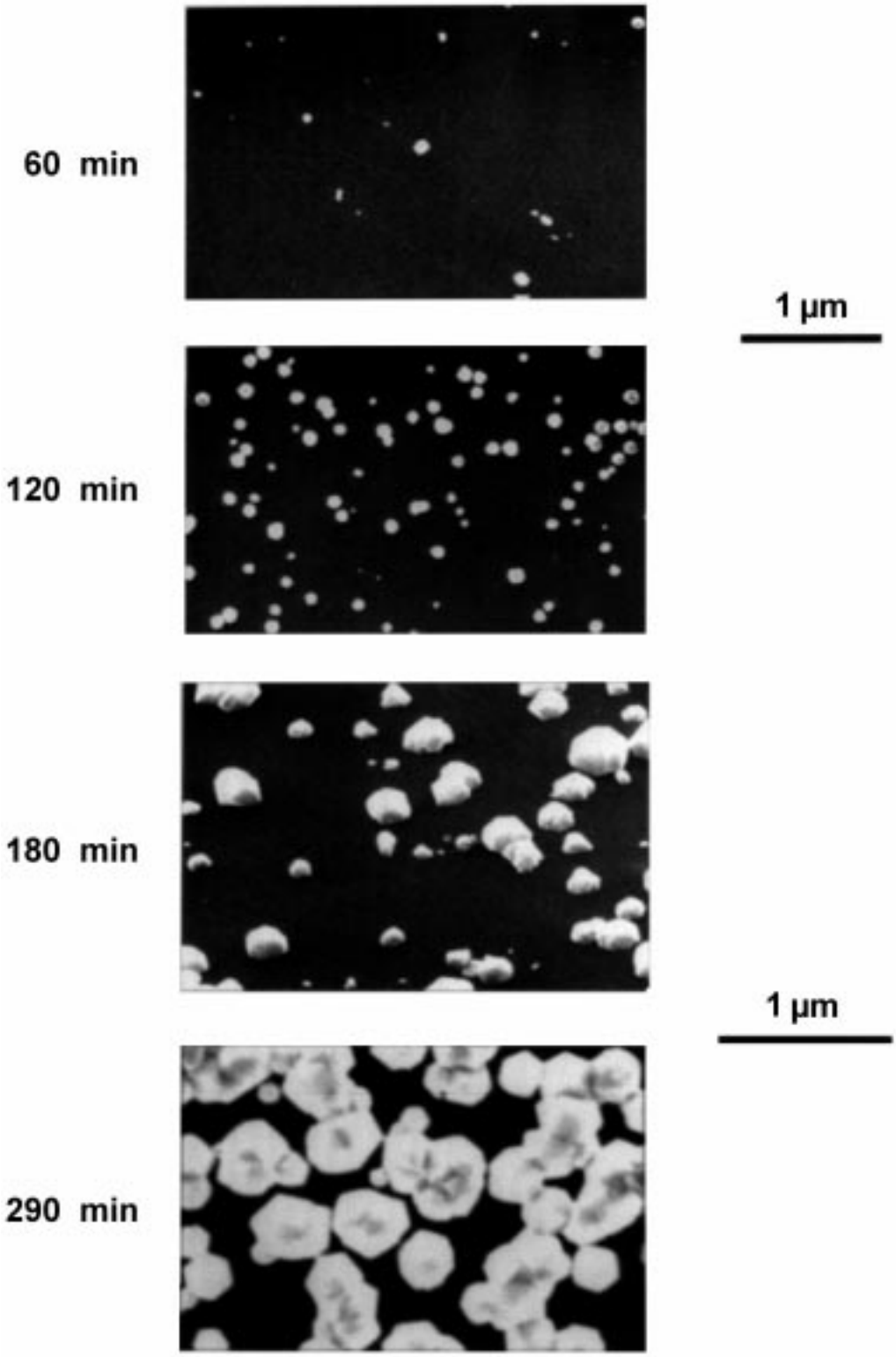

Fig. 7. SEM pictures at different deposition times. A) $t = 60$ min; B) $t = 120$ min; C) $t = 180$ min and D) $t = 300$ min. The scales are indicated on the images. In picture C, the sample is tilted.

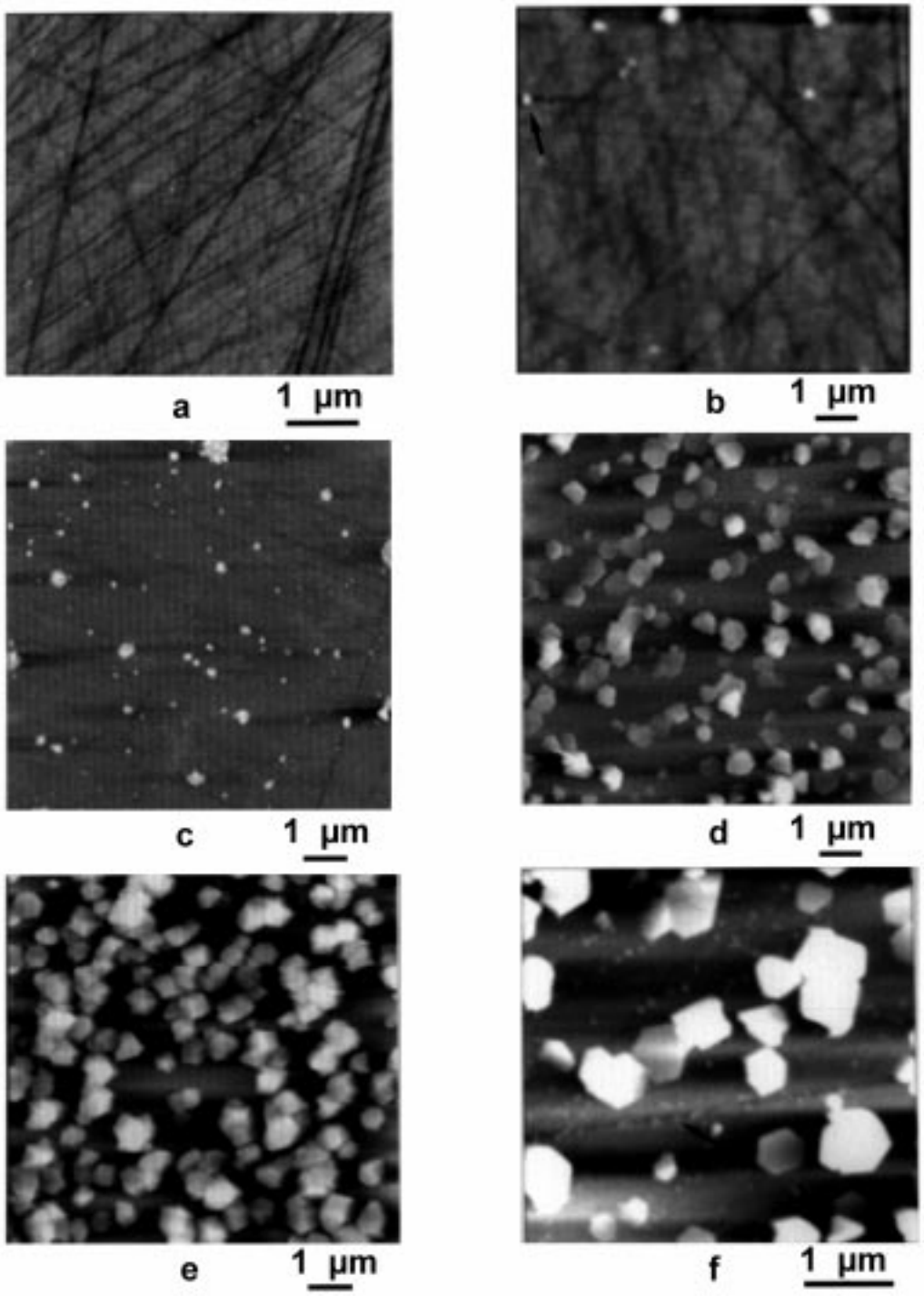

Fig. 8. AFM pictures at different deposition times. a) Initial substrate (t = 0 min); b) t = 60 min; c) t = 120 min; d) t = 180 min; e) t = 300 min and f) details of t = 180 min revealing the double distribution of growing diamond nuclei and small particles. The scales are indicated at the bottom of each picture.

as counted by AFM. It also exhibits a maximum around 60 minutes but without any incubation time. The density of small particles n is one to two orders of magnitude larger than the density of diamond nuclei N (Fig. 11).

The evolution of the height (h) to true diameter ($D_{\rm true}$) ratio, $h/D_{\rm true}$, can provide us useful information on the actual morphology of the small particles. From the AFM images, the lateral size $D_{\rm meas}$ and the height h of the islands are measured. Then, after a correction of the tip curvature effect, according to equations (3) and (4), we plot the ratio $h/D_{\rm true}$ *versus* height h for many particles within the height range 0-50 nm and for deposition times up to 120 minutes (Fig. 12). The observed behaviour is roughly linear up to $h \approx 100$ nm. Hence,

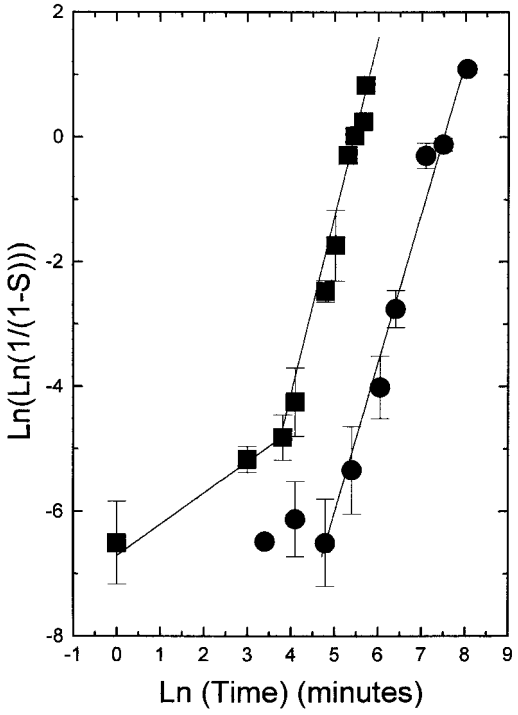

Fig. 9. Evolution of the covered surface with the deposition time in an Avrami plot $\ln(\ln(1/(1-S))) = f(\ln(t))$. (Square): scratched sample Si(100); (Circle): virgin sample Si(100) taken from [21]. The results are fitted with expression (5).

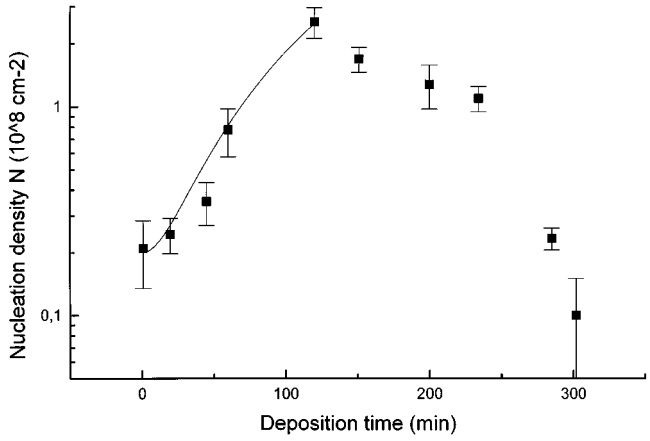

Fig. 10. Evolution of the nucleation density N with the deposition time. Full square: experimental measurements; full line: result of a fit according to equation (A.2) within the time range 0-120 minutes.

for the smallest islands, the shape is far from a cubic one ($h/D = 1$) and the exploitation of the AFM images allows us to plot a shape factor *versus* the height of these islands. This behaviour of the $h/D_{\rm true}$ ratio *versus* height reveals a particular growth mode of the small particles ($h < 100$ nm). If $h/D_{\rm true} \alpha\, h$, it leads to $D_{\rm true} = $ const. Such a condition is verified in a columnar growth along the direction h. More accurately, the set of experimental points can be inserted inside a cone that intersects the

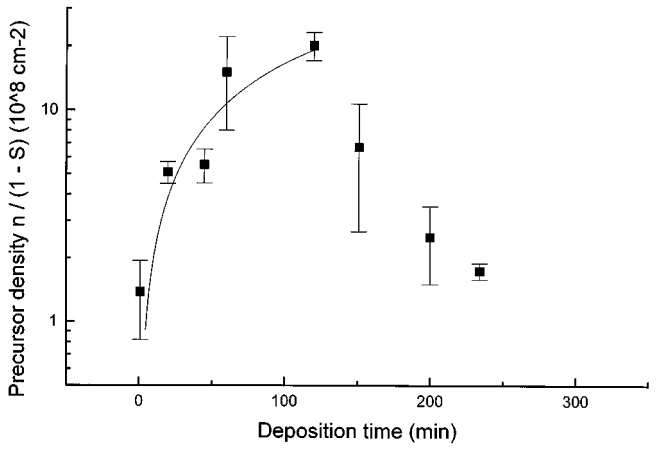

Fig. 11. Evolution of the density of the small particles on the area uncovered by diamond islands, $n/(1-S)$, with deposition time. Full square: experimental AFM measurements; Full line: result of a fit according to equations (A.1) and (5).

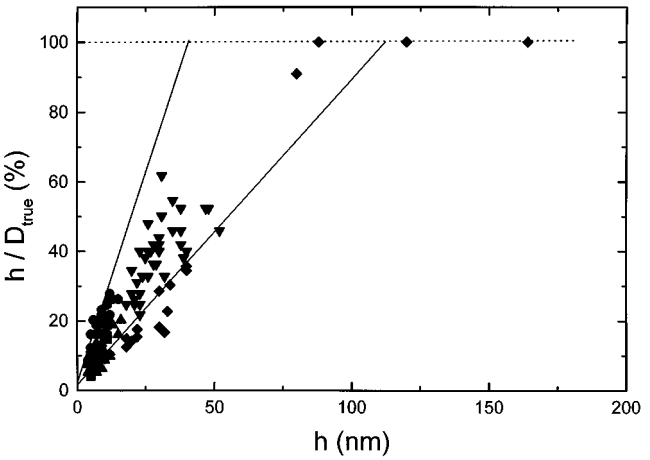

Fig. 12. Evolution of the $h/D_{\rm true}$ ratio as a function of the height h of the small islands. $D_{\rm true}$ is the diameter calculated from AFM images according to equations (3) and (4). Square: initial surface; Triangle up: 20 min; Circle: 120 min; Triangle down: 180 min; Diamond: George *et al.* [31].

line $h/D_{\rm true} = 1$ at $h_{\rm inf} = 40$ nm and $h_{\rm sup} = 120$ nm, respectively, which correspond to the lower and upper limits of the lateral size of the small particles. For the growing nuclei, *i.e.* $h \geq 100$ nm, we observe a widespread dispersion of this ratio between 0.5 and more than one, as it can be expected from facetted particles where the measurements depend on the orientation of the surface relative to the substrate. But this ratio generally tends towards 1 for the larger crystallites. Therefore, the points above 100 nm are not shown. In the same figure, we also report the AFM data of a previous study [31] in which diamond islands were obtained by microwave assisted CVD (MWCVD) on a monocrystalline Si(100) scratched with diamond paste. Their results fall within the cone of our experimental data. Above 90 nm, they also report

a constant h/D_{true} ratio = 1 which corresponds to three dimensional facetted particles. This justifies our separation of the island distribution into two populations distinguishing between small particles ($h < 100$ nm) and growing nuclei ($h > 100$ nm). TEM observations confirm that the smallest facetted island have a lateral size of no more than 100 nm.

The evolution of the mean size (not shown), indirectly determined by SEM according to equation (1), reveals three marked steps. Beyond 120 minutes, the mean size very slowly increases. This corresponds to the intense step of nucleation (Fig. 10) with a columnar growth of the small particles. It is expected that the lateral growth at this stage occurs mainly *via* an indirect process: adsorption on the substrate, diffusion on the surface and interfacial reactivity of the carbon species. Within 120-230 minutes the growth of the nuclei is mainly linear. This is the result of the growth of isolated particles now mainly by a direct surface reactivity of the active species in the gas phase. Above 230 minutes, aggregation leads to an enhanced growth of the diamond nuclei and therefore, the size grows faster than a simple linear law.

At low diamond coverage, the indirect pathway prevails on the direct pathway. The change of growth mechanism occurs for S within 1-2%, as indicated by the change of slope in the Avrami plot (Fig. 9) in good agreement with results previously reported [26].

The substrate roughness R_{q}, determined on areas including small particles but no growing nuclei, is initially 1.5 nm and remains stable up to 120 min (2.5 nm). It further increases up to 17 nm (not shown). Let us note however that the measurements at the coalescence step are less accurate and less reproducible, due to the small areas of bare silicon left on the surface.

TEM investigations of replica of the deposits showed, apart from diamond islands, shreds of silicon carbide layers. This phase is oriented with respect to the silicon substrate. The diffraction pattern clearly reveals a cubic β-SiC (100) orientation (Fig. 13). The most intense spots correspond to measured distances of 0.220, 0.153 and 0.109 nm instead of 0.220, 0.154 and 0.109 nm attributed to the (200), (220) and (400) spots for β-SiC. This is in good agreement with previous *in situ* X-ray photoelectron diffraction (XPD) measurements [41]. On the other hand, the small particles above, displayed by AFM and SEM, cannot be observed. We believe it is due to the preparation method of TEM samples: either they are dissolved with the silicon substrate or they are not removed together with the amorphous carbon layer.

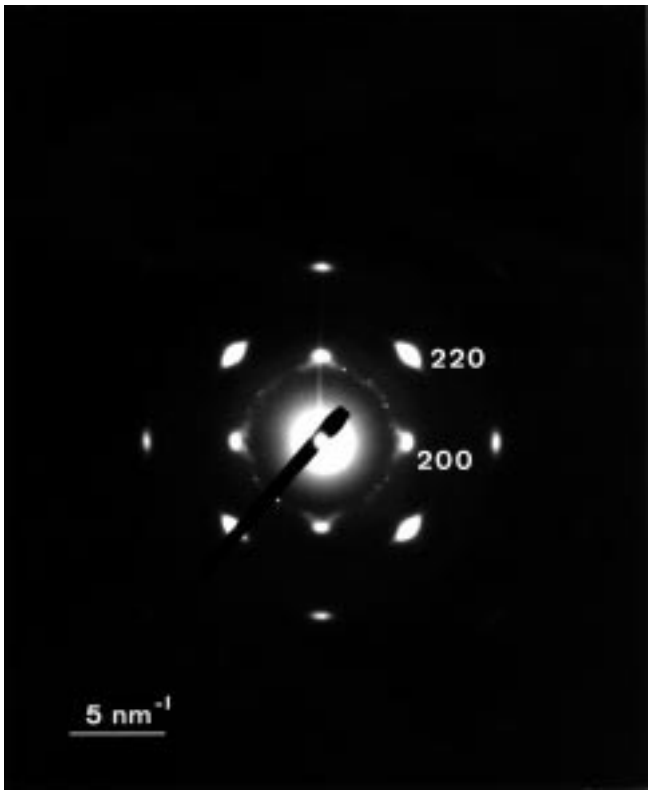

Fig. 13. Selected area diffraction showing the β-SiC (100) patterns.

4 Discussion

Before entering the discussion about the nucleation process of CVD diamond, it appears useful to define some important terms which will be used below to describe the nucleation steps. According to the abundant preexisting literature on the subject, we can distinguish two pathways for the growth of CVD diamond. They are summarized in Scheme 2.

The first one occurs through preexisting *germs* introduced by the *ex situ* pretreatment of the substrate. These germs are seeds of diamond or other abrasive ceramics left by the mechanical polishing. It must be stated however that not all the germs are suitable for diamond growth, some of them can be unactivated, due to likely competitive transformation, such as dissolution or etching as nicely reported by Maeda *et al.* [13]. These authors monitored the diamond growth on a mechanically scratched silicon surface. They were able to observe the same area at successive stages of the growth by high resolution SEM. They concluded that the diamond growth only occurred on the larger seeds left by the surface pretreatment.

The second pathway is a stepwise nucleation process. It includes first the formation of nucleation sites which are chemically and geometrically defined onto which the subsequent steps of nucleation will occur. These nucleation sites can be created either by the preliminary *ex situ* pretreatment of the substrate, and hence will be named *extrinsic nucleation sites*; or they are created *in situ* under CVD conditions and hence will be named *intrinsic nucleation sites*. Onto these nucleation sites can be formed *embryos*. These are carbon-containing phases (carbide, graphitic, diamond-like or amorphous carbon, ...) formed during *in situ* CVD. They are the precursors for diamond nucleation. They are not stable and, as such, are submitted to competitive processes such as carbon dissolution, carbon transformations

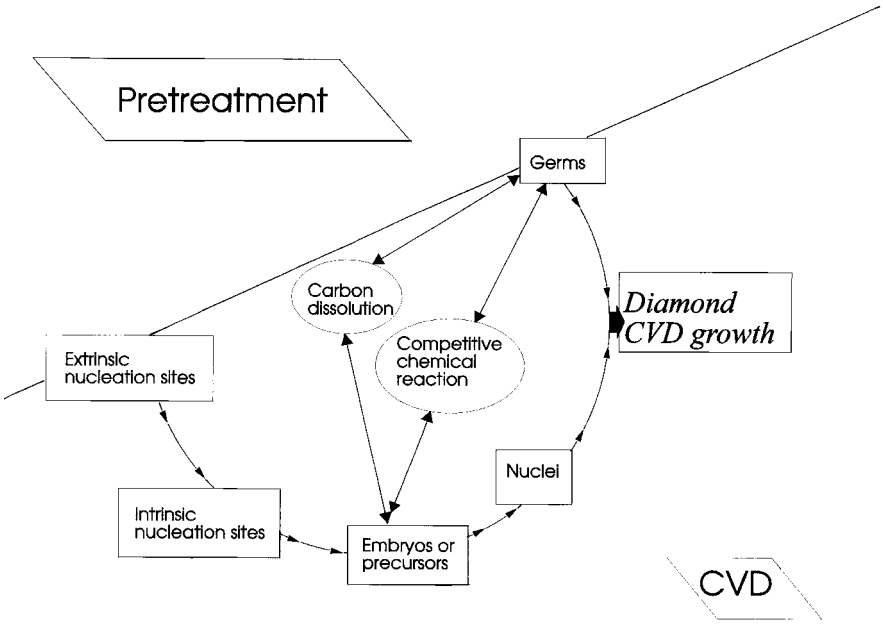

Scheme 2. The two pathways to diamond CVD growth.

(carburization, graphitization, amorphization, ...). Hence, they are strongly dependent on both the gaseous environment and the nature of the substrate. By contrast, *nuclei* are stable diamond of the smallest size issued from the embryo. At last the *growing diamond islands* arise both from the seeding and the nucleation pathways (Scheme 2).

Finally we can note the following considerations from Scheme 2:

- It must be bear in mind that both germs and embryos are submitted either to chemical reactivity, such as allotropic carbon transformation, amorphization, carbide formation or to carbon dissolution into the substrate in close competition with diamond nucleation and growth.
- Finally at each of these steps, etching is believed to occur. This is due to the high reactivity of the gas phase radicals with the substrate as well as with carbon-containing species such as germs, embryos, nuclei and growing diamond islands.

The morphology of the deposits has been studied by structural probes, whereas the nature of carbon species has been studied by electron spectroscopies (XPS, AES, ELS). By XPS the following species are observed: silicon, silicon oxide, silicon carbide and elemental carbon. Let $I(\mathrm{SiC})$, $I(\mathrm{CSi})$ be the intensities of the silicon carbide on the Si $2p$ core level (line A2, Fig. 1) and on the C $1s$ core level (line B1, Fig. 2), respectively, and $I(\mathrm{C})$ and $I(\mathrm{Si})$ the intensities of the elemental carbon (line B2, Fig. 2) and silicon (line A1, Fig. 1), respectively. As previously reported [26], both the growth of the silicon carbide layer and the diamond coverage can be extracted from the intensity of each contribution of the Si $2p$ and C $1s$ core levels. By the use of a simple model, it is possible to evaluate an equivalent thickness z of the silicon carbide layer assuming an homogeneous layer [26]. The variations of z and of the XPS intensity ratio $I(\mathrm{C})/I(\mathrm{Si})$ are reported in Figures 14 and 15, respectively. We shall discuss the occurrence of the different pathways displayed in Scheme 2 at the light of these graphs.

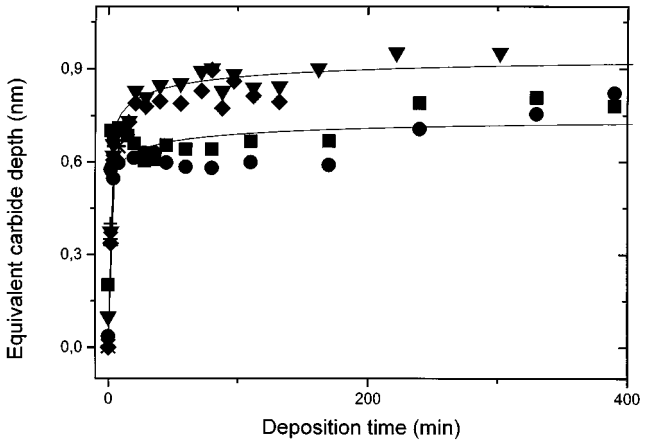

Fig. 14. Evolution of the equivalent homogeneous depth z of the silicon carbide layer with the deposition time. Scratched Si(100): Triangle down and star: Si $2p$ core level; Diamond and cross: C $1s$ core level. Virgin Si(100): full square: Si $2p$; full circle: C $1s$. The solid lines are only guides for the eye.

One pathway on Scheme 2 relies upon the presence of germs left on the surface by the pretreatment. We indeed find an initial C $1s$ contribution attributable not only to contamination carbon but also to diamond residues. More, particles are seen by AFM and SEM on the silicon surface before deposition. Some of these seeds remain stable as the CVD conditions are established and therefore are prone to further diamond growth. As the growth occurs

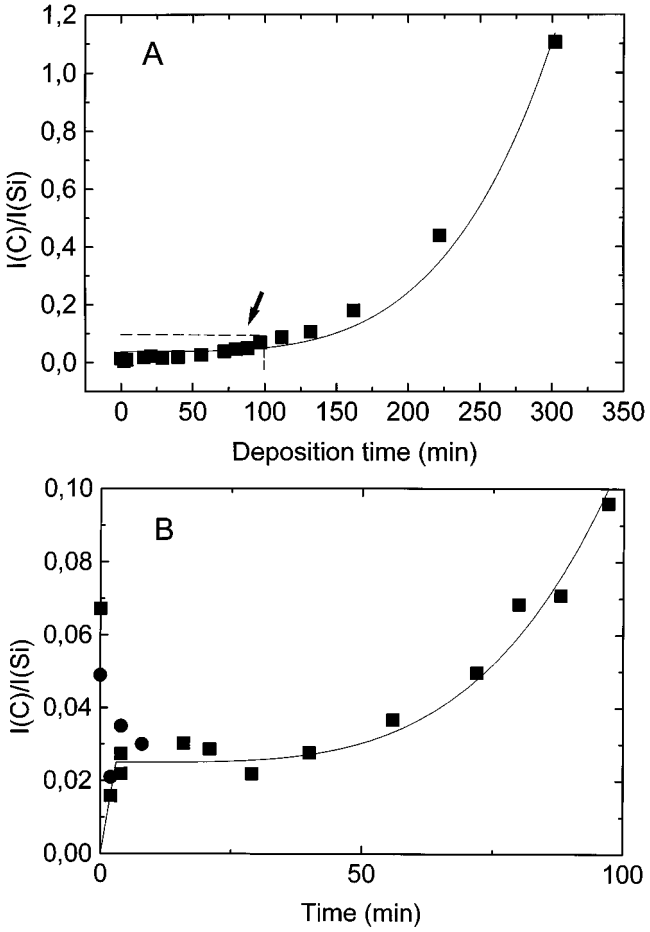

Fig. 15. Evolution of the $I(\mathrm{C})/I(\mathrm{Si})$ ratio with the deposition time. The solid line is the result of the fit of the equivalent expression taken from reference [26]. Squares and circles are the result of two independent experiments. A) Full time scale of deposition; B) focus over the first 100 minutes.

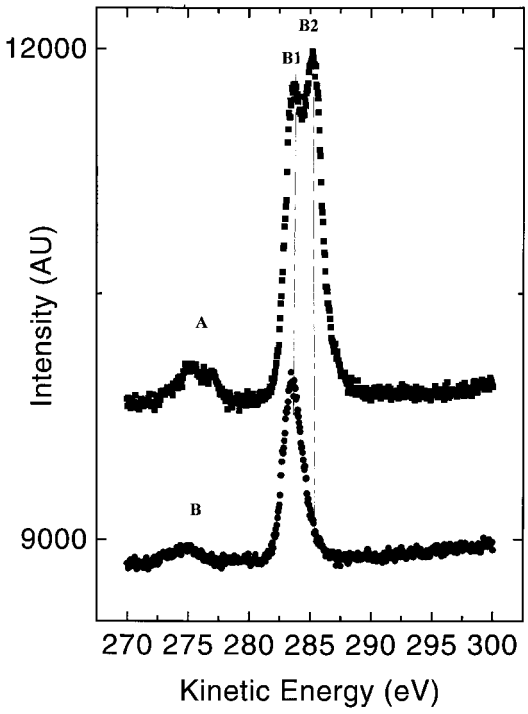

Fig. 16. C 1*s* core level of A) CVD diamond deposition (T = 1073 K; t = 170 min) B) Further vacuum treatment (T = 1323 K; t = 25 min).

directly from these germs, the initial density of diamond islands is not zero. However we believe that the smallest germs may also be dissolved into silicon or transformed into carbide in the CVD conditions. This assertion is supported by the initial decrease of the XPS carbon signal $I(\mathrm{C})/I(\mathrm{Si})$ reported in Figure 15B. Moreover the following experiment points out to the reversible character of the transformation between diamond islands on a silicon substrate and silicon carbide. After an exposure to the CVD conditions at 1073 K during 170 min, the C 1*s* core level displays the B1 and B2 lines characteristic of silicon carbide and diamond, respectively (Fig. 16). Further vacuum treatment during 25 min at 1373 K leads to complete removal of the diamond feature, indicating a redissolution of the diamond islands at elevated temperatures with formation of silicon carbide.

The germ pathway is very often rightly invoked in the literature as the main pathway to diamond generation in CVD conditions. However we believe this cannot be the only process in our conditions. Indeed the density of diamond islands does not remain constant, but increases after some incubation time (Fig. 10). The Avrami plot (Fig. 9) also indicates that the nucleation rate is not null. These experimental facts prove that it is necessary to consider now a nucleation mechanism.

The first process to consider is the formation of nucleation sites either by a previous or *in situ* pretreatment leading to extrinsic and intrinsic nucleation sites, respectively. Indeed, on silicon, the role of the preformed surface defects in the nucleation processes has been emphasized: apex of silicon pyramids [9], sharp edges [42], whiskers [10], edges of terraces [11]. In a study on a chemically etched silicon surface containing large terraces, we noted that most of the diamond nuclei preferentially nucleate on the edges of some terraces [43]. The reasons why these sites are preferred for the nucleation remains unclear but it has been explained either (i) by a minimization of the interfacial energy [42] or (ii) by the presence of more dangling bonds enhancing the energy of chemisorption [43] or (iii) by a more rapid carbon saturation on these sites [44], due to the annihilation of the surface diffusion of the carbon species.

In our conditions, the only preexisting surface defects lie along scratch lines. On the whole, there is no obvious correlation between diamond nuclei and scratch lines. Therefore we are inclined to minimize here the role played by extrinsic nucleation sites. No definite conclusions can be taken however as: (i) the limited resolution of the AFM tip blinds small scratch lines and (ii) these lines can be partly transformed into intrinsic nucleation sites *via* either

carbon adsorption or silicon carbide formation or silicon etching. Silicon etching by radical hydrogen and silicon redeposition lead to an increase of the surface roughness by creation of holes and pits, respectively. Holes of threefold and fourfold symmetry are found on pristine Si(111) and Si(100), respectively [21,45]. These surface defects may provide proper geometric sites for further diamond nucleation. In addition, it is tempting to assign the small particles to such silicon protrusions, clearly detected both by SEM and AFM. At the present time, the chemical nature of these small particles is not clearly elucidated. Previous studies about diamond growth on silicon reported the existence of such a double distribution [46,47]. But, surprisingly, the nature of these small particles has been little discussed in the literature and, when tempted, the interpretations are quite contradictory. A Raman study would have given evidence for polyacethylene nanocrystals [48], while β-SiC particles are invoked elsewhere [46]. A more recent and careful HRTEM study revealed silicon protrusions [49]. A columnar mode of growth of these protrusions is expected by an etching-redeposition process which is effectively observed by AFM. We failed to detect them by TEM while preparing the sample by a replica technique that dissolves silicon, which is consistent with the silicon nature of these protrusions. TEM observations of these small particles, by the way of another preparation technique, are presently under active investigations. Whatever the interpretation, the absence of accurate structural characterization of these protrusions left still obscure this important step of the nucleation mechanism.

Now can these small particles be intrinsic nucleation sites to diamond nucleation? Some indications support this assertion. Hence the kinetics of the density of these small particles, which display no incubation time unlike diamond nuclei but display a maximum, would indicate that they will be precursors to the diamond nucleation. We therefore develop a crude model, derived from the Molinari model [50] (Appendix 1) to account for the kinetics of both the density of these small particles $n(1-S)$ and the density of diamond islands N. This model is developed in Appendix 1, assuming that the aggregation of the growing nuclei is negligible. This model accounts, within the first 120 minutes, of both the orders of magnitude and the trends of the evolution of the density of small particles and growing nuclei. Hence the density of small particles on uncovered area $n(1-S)$ passes through a maximum as it is an intermediary step in the global kinetic scheme of nucleation (Scheme 3 in Appendix). Moreover the probability for these precursors to become a diamond island can be roughly determined from the ratio of the densities $N(1-S)/n$, and is estimated to around 10%. It is however highly unlikely that diamond might directly nucleate on silicon. This has sometimes been claimed, yet in the case of instantaneous nucleation like polarisation-enhanced nucleation [51] or at high carbon concentration [52]. More likely, diamond can nucleate either on silicon carbide or on amorphous DLC carbon [52–54]. The occurrence of one of this two pathways depend on the experimental CVD conditions: substrate temperature, carbon content... We will discuss the probability of their occurrence in our case.

Many authors report the formation of silicon carbide [35,49,55–57]. The questions which remain unsolved however are: (i) does this silicon carbide homogeneously cover the surface? and (ii) does silicon carbide behave as a precursor of diamond nucleation? From the spectra of Figures 1 and 2, we show that it is possible to monitor the growth of the equivalent depth of silicon carbide layer z, assuming an homogeneous repartition [26]. The depth z can be extracted by two ways from the ratio of the C $1s$ (I(CSi)) or the Si $2p$ (I(SiC)) signals to the Si $2p$ I(Si) signal, respectively:

$$z(\mathrm{Si}) = \lambda_{\mathrm{SiC}} \cos\theta \ln\{1 + [I(\mathrm{SiC})/I(\mathrm{Si})]\} \quad (6)$$

$$z(\mathrm{C}) = \lambda_{\mathrm{aver}} \cos\theta \ln\{1 + [\lambda_{\mathrm{SiC}} I(\mathrm{CSi})/\lambda_{\mathrm{CSi}} I(\mathrm{Si})]\} \quad (7)$$

where the signals are corrected for the photoemission sensivity factors, the transmission function of the analyzer, the asymmetric factor of the core level, the atomic density and the mean free paths in silicon carbide at the Si $2p$, the C $1s$ and the average kinetic energies, which are λ_{aver}, λ_{SiC} and λ_{CSi}, respectively (Fig. 14).

Although the curves are quite similar, we note slightly but systematically lower z values when extracted from the C $1s$ core level rather than from the Si $2p$ core level. This can be explained by an inappropriate choice of the mean electron escape depth in silicon carbide. At higher deposition times, the sensitivity on the C $1s$ core level becomes very weak and the error is important. The main point is a rapid increase of the silicon carbide contribution which reaches a steady level after less than 20 minutes. This depth z_∞ is around 1.0 ± 0.1 nm, a value which is probably slightly underestimated as we include the small signal of substoichiometric silicon oxide in the overall signal of the substrate. For comparison, we also report the same parameter on virgin Si(100). Lower values are obtained which means that the silicon carbide layer is thinner ($z_\infty \approx 0.7 \pm 0.1$ nm). Equations (6) and (7) assume a continuous silicon carbide layer.

Actually, the chemical nature, the crystallinity and the homogeneity of the intermediate layer strongly depend on the CVD experimental conditions. As an illustration, an increase of the methane content in the gas phase from 0.3 to 2% induces a transition from a single-crystal layer of β-SiC to an amorphous carbon layer [52]. In some cases, continuous layers of silicon carbide were observed [55,56], while other studies pointed out to the presence of nanocrystals of carbide [49,57]. This XPS study cannot elucidate the problem of a homogeneous or heterogeneous repartition of silicon carbide. However, the observation of replica films by TEM shows shreds of silicon carbide and suggests a discontinuous repartition of the silicon carbide onto the substrate. Moreover, it is expected that the silicon protrusions displayed above are carburized on top. This ensemble may act as an embryo to the diamond nucleation. A recent HRTEM study of diamond crystallites grown onto a silicon substrate [50] supports this conclusion. Evidence is given for silicon pitches of 10−15 nm lateral size onto which a thin layer of silicon carbide (2 nm

thick) and further diamond are formed. In our present case, the AFM study of such embryos allows us to measure their dimensions: the lateral size D_{true} and the height h, and to give insight to their growth mode. The linear relationship between h/D_{true} and h leads to a columnar growth of the embryos (Fig. 12). For diamond nuclei of lateral size D_{true} larger than 100 nm, the h/D_{true} ratio is close to one, the growth in the island mode becoming now isotropic. This is in good agreement with the Avrami plot which shows a second regime where the growth is governed by direct impingement from the vapor phase. Both the clean silicon surface and the grooves left by the scratching undergo an etching process by the radical hydrogen of the gas phase leading to a roughening of the silicon sample [45]. The preferential growth of silicon carbide on top of redeposited silicon protrusions may explain why we could not observe these embryos by HRTEM due to the removal of the silicon during the replica procedure. Onto these silicon carbide nanocrystals, the nucleation of diamond is possible with a weak probability ($\approx 10\%$). On the other hand, the nucleation probability is practically null on clean SiC [51].

Yugo *et al.* [46,58], interpreting STM images, reported a size effect upon diamond nucleation. According to them, the proper sites for diamond nucleation are surface defects of both comparable size and shape to critical diamond nuclei. In standard CVD experimental conditions, they estimated this critical size to several nanometers. This is in line with our interpretation if we consider that the lateral size of the protrusions determine the critical size of diamond nuclei.

The other possible carbon precursor for diamond nuclei is amorphous DLC carbon. Previous studies by TEM and EELS [53,54] report the formation of a thin amorphous layer at the interface of silicon and CVD diamond. At this stage, it is instructive to compare the 250 eV ELS spectra (Fig. 6), on pristine and scratched silicons. In the energy range of 5–15 eV, particularly sensitive to the carbon bonding states, the difference spectrum exhibits a higher contribution for the scratched sample. Therefore, we believe the formation of diamond-like carbon on top of protrusions could not be excluded.

Finally, travelling on the lower branch of Scheme 2 after formation of nucleation sites and carbon-based embryos on it, we reach the nucleation step. Models have described the diamond formation from either silicon carbide [51] or amorphous DLC carbon [59]. It is speculated that diamond nucleation occurs on top of silicon protrusions covered either by silicon carbide or DLC amorphous carbon. At this state, some remarks can be made:

The size of the diamond nuclei must be larger than a critical size which is equal to the lateral size of the silicon protrusions. Hence we fail to observe by TEM, SEM and AFM diamond nuclei of size lower than several nanometers.

The nucleation kinetics displays two major steps (Fig. 10), the first one at $3 \times 10^7/\text{cm}^2$, is reached after 50 minutes while a rapid transition to $10^8/\text{cm}^2$ occurs between 100 and 150 minutes of deposition. This incubation time of 50 minutes corresponds to the time of formation of the precursors.

This time of incubation is probably related to the stabilization of the proper nucleation sites, both on a geometrical and a chemical point of view and the formation of precursors. According to our results, this time is within the 0–100 minutes range. Above this time range we indeed observe the increase in the XPS ratio $I_{\text{D}}/I_{\text{Si}}$ evolution (Fig. 15) as well as in the surface roughness measured by AFM.

A model with several steps was already postulated by Stiegler *et al.* [60] to modelize the diamond MWCVD growth on a Si(100) scratched surface. The authors determined three main stages from the plot of the diamond nuclei density: the first one which occurred very quickly is attributed to the growth of diamond on the seeds left by the mechanical polishing. According to the authors, only the larger-sized seeds grew in agreement with the Maeda's study [13]. A second step is related to the classical nucleation process while the last one is called "avalanche period" and should be due to an increase of the local carbon concentration in the vicinity of the diamond growing islands [59]. We cannot observe this third step as it is not easily detectable and therefore we do not discuss it. On the other hand, we found no mention of no-facetted small particles coexisting with diamond islands. These authors conclude that in their case the main process is rather a seeding than a nucleation process.

5 Conclusion

The formation of diamond by a CVD process on Si(100) has been explained in the framework of two pathways.

A *seeding pathway* occurs by direct growth from a part of the diamond seeds left by the mechanical pretreatment. Not all of these seeds however are prone to diamond growth as they can be partly dissolved and carburized.

A *nucleation pathway* is a stepwise process including the formation of extrinsic (pretreatment) or intrinsic (*in situ*) nucleation sites, and subsequent formation on it of carbon-based precursors before further diamond nucleation. It is believed that nucleation sites could be either grooves of scratching lines or protrusions of size lower than 100 nm produced by an etching- redeposition process of silicon. On top of these protrusions as well as on the bare substrate, a thin layer of silicon carbide, 1 nm thick, rapidly forms. Diamond-like carbon is also likely present. Diamond nucleation can occur at the end of this stepwise process. It is highly probable that the nucleation includes both a proper nucleation site and the complex growth of a carbon-based precursor which is more enriched in carbon and densified as the process runs. The chemical and structural nature of these precursors to diamond nucleation is at the present time under active investigations.

We are grateful to Dr R. Polini (Univ. Tor Vergata, Roma) for the SEM observations and to Dr B. Lang for useful discussions. Dr R. Michelangelo is greatly acknowledged for performing the image analyses by the Khoros freeware.

Appendix

By contrast with most of the literature, we fail to fit with an exponential line the evolution of the growing diamond nuclei. In the literature, there are some reports of an incubation time and there is a model developed by Molinari *et al.* [51] which supposes the formation of embryos before nucleation starts. It is not the topic of this appendix to discuss the real nature of these embryos. Assuming that (i) some seeding is likely, yielding an initial nucleation density N_0; (ii) nucleation sites are provided along the edges and corners of the mechanical scratches with density N_s and (iii) small particles are formed on such sites which are precursors of diamond nucleation, it is possible then to reconsider the model of Molinari *et al.* We further assume that (i) when starting the nucleation step, the covered surface S is small so that any capture by the growing diamond nuclei is negligible and (ii) the reverse reaction of precursor annihilation is negligible relative to the formation of such precursor. These assumptions may be considered as valid beyond 120 minutes where both the surface coverage is small (Fig. 9) and very few aggregation occurs (Figs. 7 and 8). Hence the densities of the precursor $n/(1-S)$ and of the growing diamond nuclei N can be expressed by formula (A.1) and (A.2), respectively:

$$n(t) = k_e N_S \frac{[\exp(-K_D t) - \exp(-k_e t)]}{[(k_e - K_D)(1-S)]} \quad \text{(A.1)}$$

$$N(t) = N_0 + N_S \frac{1 + [(K_D \exp(-k_e t) - k_e \exp(-K_D t))]}{(k_e - K_D)} \quad \text{(A.2)}$$

where k_e and K_D are the kinetic rates of the precursor and the growing diamond nuclei formation ($k_e > K_D$) as displayed in Scheme 3.

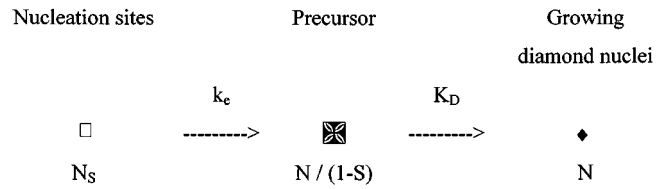

Scheme 3. Kinetic model of the steps of diamond nucleation.

Figures 10 and 11 display fits of the growing nuclei and precursor densities for the same set of parameters N_S, k_e and K_D. For both curves, the agreement is rather satisfactory with respect to shape and order of magnitude. Due to the simplifications included in this crude model, we believe that the values extracted must however be handled with care and only the trends and the order of magnitude may be significant. Above 120 minutes, both aggregation of the growing nuclei and capture of the precursor by the growing nuclei occur and no attempt had been carried out to fit the complex evolution of the densities.

References

1. K.E. Spear, J.P. Dismukes, in *Synthetic diamond: emerging CVD science and technology* (The electrochemical society, J. Wiley and Sons, 1994).
2. S. Matsumoto, Y. Sato, M. Tsutsumi, N.J. Setaka, Mat. Sci. **17**, 3106 (1982).
3. J.C. Angus, A. Argoitia, R. Gat, Z. Li, M. Sunkara, L. Wang, Y. Wang, Trans. Phil. Mag. A **342**, 195 (1993).
4. W.A. Yarbrough, J. Am. Ceram. Soc. **75**, 3179 (1992).
5. Y. Bar Yam, T.D. Moustakas, Nature **342**, 786 (1989).
6. D.R. Frankl, J.A. Venables, Adv. Phys. **19**, 409 (1971).
7. B. Lewis, J.C. Anderson, *Nucleation and Growth of thin Films* (Academic Press, New York, 1978).
8. J.A. Venables, G.D.T. Spiller, M. Hanbucken, Rep. Progr. Phys. **47**, 399 (1984).
9. R. Ramesham, C. Ellis, J. Mat. Res. **7**, 1189 (1992).
10. E.I. Givargizov, V.V. Zhirnov, A.V. Kuznetsov, P.S. Plekhanov, Mater. Lett. **18**, 61 (1993).
11. R. Polini, J. Appl. Phys. **72**, 2517 (1992).
12. S. Iijima, Y. Aikawa, K. Baba, Appl. Phys. Lett. **57**, 2646 (1990).
13. H. Maeda, S. Ikari, T. Okubo, K. Kusakabe, S. Morooka, J. Mat. Sci. **28**, 129 (1993).
14. B.R. Stoner, G.H.M. Ma, S.D. Wolter, J.T. Glass, Phys. Rev. B **45**, 11067 (1992).
15. J.C. Angus, M. Sunkara, S.R. Sahaida, J.T. Glass, J. Mater. Res. **7**, 3001 (1992).
16. W.R.L. Lambrecht, C.H. Lee, B. Segall, J.C. Angus, Z. Li, M. Sunkara, Nature **364**, 607 (1993).
17. B. Lux, R. Haubner, *Diamond and diamond-like films*, edited by R.E. Clausing *et al.* (Plenum Press, New York, 1991).
18. L. Demuynck, F. Bigorgne, B. Carrière, A. George, J.P. Michel, F. Le Normand, Diamond Rel. Mat. **3**, 569 (1994).
19. D.N. Belton, S.J. Schmieg, Surf. Sci. **233**, 131 (1990).
20. S.J. Harris, D.N. Belton, A.M. Weiner, S.J. Schmieg, J. Appl. Phys. **66**, 5353 (1989).
21. L. Demuynck, Ph.D. thesis, University of Strasbourg, France 1995.
22. E. Molinari, R. Polini, M. Tomellini, Appl. Phys. Lett. **61**, 1287 (1992).
23. R. Polini, M. Tomellini, Diamond and Rel. Mat. **4**, 1311 (1995).
24. J. Rankin, R.E. Boekenhaven, R. Csencsits, Y. Shigesato, M.W. Jacobsen, B.N. Sheldon, J. Mat. Res. **9**, 2164 (1994).
25. J.W. Kim, Y.J. Baik, K.Y. Eun, N. Yoon, Thin Solid Films **212**, 104 (1992).
26. F. Le Normand, J.C. Arnault, L. Fayette, B. Marcus, M. Mermoux, V. Parasote, J. Appl. Phys. **80**, 1830 (1996).
27. X. Jiang, K. Schiffmann, C.P. Klages, Phys. Rev. B **50**, 8402 (1994).
28. L. Constant, B. Prévôt, F. Le Normand (submitted).
29. L. Constant, C. Speisser, F. Le Normand, Surf. Sci. **387**, 28 (1997).
30. D. Morar, F.J. Himpsel, Phys. Rev. B **33**, 1340 (1985).
31. M.A. George, A. Burger, W.E. Collins, J.L. Davidson, A.V. Barnes, N.H. Tolk, J. Appl. Phys. **76**, 4099 (1994).
32. D.N. Belton, S.J. Harris, A.M. Weiner, S.J. Schmieg, T.A. Perry, Appl. Phys. Lett. **54**, 416 (1989).
33. T.M. Parrill, Y.W. Chung, Surf. Sci. **243**, 96 (1991).
34. F.R. Mac Feely, S.P. Kowalczyk, L. Ley, R.G. Cavell, R.A. Pollak, D.A. Shirley, Phys. Rev. B **9**, 5268 (1974).

35. L. Demuynck, J.C. Arnault, R. Polini, F. Le Normand, Surf. Sci. **377**, 871 (1997).
36. B. Lang, P. Scholler, B. Carrière, Surf. Sci. **99**, 103 (1980).
37. L. Demuynck, F. Le Normand, Phys. Stat. Sol. (a) **161**, 217 (1997).
38. D.R. Wheeler, S.V. Pepper, Surf. Interf. Anal. **10**, 153 (1987).
39. M. Avrami, J. Chem. Phys. **7**, 1103 (1939).
40. J.W. Christian, *Theory of transformation in metals and alloys* (Pergamon Press, London, 1975).
41. E. Maillard-Schaller, O.M. Kuettel, P. Gröning, P. Aebi, L. Schlapbach, Diam. Rel. Mat. **6**, 282 (1997).
42. P.A. Dennig, D.A. Stevenson, Appl. Phys. Lett. **59**, 1562 (1991).
43. J.C. Arnault, M. Hanbücken, C. Speisser, F. Le Normand (to be published).
44. K. Kobayashi, N. Mutsumura, Y. Machi, Mater. Manufacturing Processes **7**, 395 (1992).
45. J.C. Arnault, S. Hubert, F. Le Normand, J. Phys. Chem. B **102**, 4856 (1998).
46. S. Yugo, T. Kimura, H. Kanai, *Science and Technology of New Diamond*, edited by Saito S., Fukunaga O., Yoshikawa M. (Tokyo, 1990), p. 119.
47. H. Liu, D.S. Dandy, *Diamond chemical vapor deposition* (Noyes publications, Park Ridge, 1995).
48. T. Lopez-Rios, E. Sandré, S. Leclercq, E. Sauvain, Phys. Rev. Lett. **76**, 4935 (1996).
49. W. Jäger, D. Wittorf, C.L. Jia, U. Urban, in *Proceedings 9th CIMTEC*, 1998, edited by P. Vincenzini (to be published).
50. E. Molinari, R. Polini, M. Tomellini, Appl. Phys. Lett. **61**, 1287 (1992).
51. P. Mahalingam, H. Liu, D.S. Dandy, J. Appl. Phys. **81**, 1966 (1997).
52. B.E. Williams, J.T. Glass, R.F. Davis, K. Kobashi, J. Crystal Growth **99**, 1168 (1990).
53. Y. Tzou, J. Bruley, F. Ernst, M. Ruhle, R. Raj, J. Mater. Res. **9**, 1566 (1994).
54. N. Jiang, A. Hatta, T. Ito, Z. Zhang, T. Sasaki, A. Hiraki, J. Mater. Res. **11**, 1783 (1996).
55. B.R. Stoner, G.H.M. Ma, S.D. Wolter, J.T. Glass, Phys. Rev. B **45**, 11067 (1992).
56. D.N. Belton, S.J. Harris, S.J. Schmieg, A.M. Weiner, T.A. Perry, Appl. Phys. Lett. **54**, 416 (1989).
57. S. Yugo, T. Kimura, H. Kanai, Y. Adachi, Mat. Res. Soc. Symp. Proc. **97**, 327 (1987).
58. S. Yugo, A. Izumi, T. Kanai, T. Muto, T. Kimura, in *2nd Int.Conf. on New Diamond Science and Technology* (Washington D.C., 1991), p. 385.
59. Singh J., Vellaikal M., Dat R., Thin Solid Films **238**, 133 (1994).
60. J. Stiegler, Y. Von Kaenel, M. Cans, E. Blank, J. Mater. Res. **11**, 716 (1996).